

Drift Estimation for Stochastic Differential Equations with Denoising Diffusion Models

Marcos Tapia Costa^{1,2}

Nikolas Kantas¹

George Deligiannidis²

February 23, 2026

Abstract

We study the estimation of time-homogeneous drift functions in multivariate stochastic differential equations with known diffusion coefficient, from multiple trajectories observed at high frequency over a fixed time horizon. We formulate drift estimation as a denoising problem conditional on previous observations, and propose an estimator of the drift function which is a by-product of training a conditional diffusion model capable of simulating new trajectories dynamically. Across different drift classes, the proposed estimator was found to match classical methods in low dimensions and remained consistently competitive in higher dimensions, with gains that cannot be attributed to architectural design choices alone.

1. Problem Statement

Suppose one is interested in modelling a time series as a continuous-time stochastic differential equation (SDE),

$$dY_t = \mu(Y_t)dt + \sigma dB_t, t \in [0, T], \quad (1)$$

where $(B_t)_{t \in [0, T]}$ is a D -dimensional Brownian motion and $\mu : \mathbb{R}^D \rightarrow \mathbb{R}^D$ is a time-homogeneous drift function. We assume σ is known or well-estimated, i.e., using the quadratic variation of a single path, see (Jacod, 1994; Barndorff-Nielsen & Shephard, 2002; Jacod & Protter, 2012). We also assume μ is locally Lipschitz to ensure a strong solution to (1) up to terminal time T , see (Karatzas & Shreve, 2000).

We will investigate the case we are given a dataset \mathcal{D} consisting of $I \gg 1$ i.i.d. trajectories, each with J observations of dimension D observed at times $t_j = j\Delta \forall j \in \{1, \dots, J\}$, such that $\mathcal{D} = \{Y_{t_1}^{(i)}, \dots, Y_{t_J}^{(i)}\}_{i \in [I], [I] := \{1, \dots, I\}}$ and $\Delta := t_{j+1} - t_j$ is small. In our setting, the number of trajectories I and the number of discrete observations J are fixed with a constant sampling frequency

Δ .

Without loss of generality, we assume $T = 1$ and $Y_0^{(i)} \sim Q_0$, where Q_0 admits a density with respect to the Lebesgue measure dy_0 ; $Q_0(dy_0) = q_0(y_0)dy_0$. We will study the problem of estimating the drift function μ from the dataset \mathcal{D} .

1.1. Drift estimation as a regression

Letting $Z_{t_j} := Y_{t_j} - Y_{t_{j-1}}$, the solution over $s \in [t_{j-1}, t_j]$ to (1) takes the form,

$$Z_{t_j} = \int_{t_{j-1}}^{t_j} \mu(Y_s)ds + \sqrt{\Delta} \omega, \omega \sim \mathcal{N}(0, I). \quad (2)$$

For small Δ , an Euler-Maruyama (EM) approximation to (2) above yields,

$$\widehat{Z}_{t_j} = \mu(Y_{t_{j-1}})\Delta + \sqrt{\Delta}\omega, \omega \sim \mathcal{N}(0, I) \quad (3)$$

and the drift enters μ through the conditional mean:

$$\mathbb{E} \left[\widehat{Z}_{t_j} \mid Y_{t_{j-1}} \right] = \mu(Y_{t_{j-1}})\Delta. \quad (4)$$

In our multiple trajectory setting, with $I \gg 1$, one could use (4) to learn μ by regressing states against increments through a nonparametric function D_θ (Zhao et al., 2025),

$$D_{\theta^*} = \arg \min_{\theta} \frac{1}{2} \sum_{i,j} \left[\left\| D_\theta(Y_{t_{j-1}}^{(i)}) - Z_{t_j}^{(i)} \right\|_2^2 \right]. \quad (5)$$

It is well known that in our fixed T, J, Δ setting, the drift μ cannot be estimated consistently from a single trajectory (Jakobsen & Sørensen, 2015). However, in the multiple trajectory setting, (Zhao et al., 2025) provide asymptotic convergence guarantees for separable drift functions under conditions on the class of functions D_θ . Yet, the drift estimator D_{θ^*} can suffer from high variance, as the drift contribution scales as $\mathcal{O}(\Delta)$, and the diffusion noise scales as $\mathcal{O}(\sqrt{\Delta})$ (Gobet, 2002; Kutoyants, 2004), and the Fisher information per observation vanishes as $\Delta \rightarrow 0$. In high dimensions, this difficulty is further compounded by deteriorating nonparametric regression convergence rates with dimension, requiring significantly more data to achieve the same accuracy as in lower dimensions (Tsybakov, 2009).

¹Department of Mathematics, Imperial College London, UK

²Department of Statistics, University of Oxford, UK

A general approach to mitigate variance in regression problems is to inject additive Gaussian noise into the inputs, which acts as a form of Tikhonov regularisation on D_θ (Bishop, 1995). More generally, under the loss in (5), regression with noisy inputs corresponds to learning the conditional expectation of the target given the corrupted input, i.e., learning a *denoiser*. Moreover, (Starnes & Webster, 2025) show learning the denoiser from Gaussian perturbations can smooth low variance, high curvature directions during optimisation and lead to a better conditioned stochastic gradient descent problem. (Vincent, 2011) further showed that such denoising objectives are equivalent to score matching under Gaussian perturbations. Modern denoising diffusion models extend this principle by introducing a controlled, multi-scale noising process and learning denoisers across noise levels, with great success in image and video applications (Sohl-Dickstein et al., 2015; Ho et al., 2020; Song et al., 2021b).

In this paper, we extend the methodology of denoising diffusion models to introduce a controlled noising process and derive an estimator for the drift μ . We will propose a novel construction for the estimator, and present systematic empirical results showing that the denoising-based estimator improves out-of-sample performance in high-dimensional settings with strong interactions or chaotic dynamics, while remaining competitive when standard regression already generalises well. Theoretical guarantees as in (Zhao et al., 2025) are left for future work.

2. Related Literature

2.1. Drift estimation for stochastic differential equations

The problem of estimating the drift function of an SDE has been extensively studied. In the single trajectory setting, (Kessler, 1997) derived an efficient estimator for the drift function of an ergodic scalar diffusion observed at discrete times when transition densities are unknown. (Shoji & Ozaki, 1995) developed a pseudo-likelihood estimator from a locally linear approximation of the SDE, while (Aït-Sahalia, 2002) used polynomial Hermite expansions of the transition density to obtain an approximate maximum likelihood estimator.

Nonparametric approaches were introduced through the kernel regression estimator of (Watson, 1964), and (Nadaraya, 1964) was first applied to Brownian SDEs by (Florens-Zmirou, 1993), who estimate both drift and diffusion coefficients in scalar diffusions, and (Bandi & Phillips, 2003; 2007) provided uniform convergence rates for its application to high frequency financial data. Furthermore, (Dalalyan, 2006) derived a nonparametric estimator for homogeneous drift functions that achieves minimax optimal

rates, while (Comte & Genon-Catalot, 2009; 2010) proposed penalised least squares projection methods to jointly estimate the drift and diffusion coefficients nonparametrically. More recently, (Oga & Koike, 2023) develop theoretical guarantees for multidimensional drift estimation for a class of deep neural networks, given a single path with many observations.

In the multiple trajectory setting, which is the observation regime of this paper, (Bonalli & Rudi, 2025) used a Reproducing Kernel Hilbert Space approximation of the Fokker-Planck equation to estimate multidimensional non-linear drift functions. (Mohammadi et al., 2024) use Functional Data Analysis to develop a drift estimator given sparse observations. (Marie & Rosier, 2023) extend kernel smoothing estimators of the drift function to the multiple i.i.d. trajectory setting, while (Comte & Genon-Catalot, 2020; Denis et al., 2021) extend penalised least squares estimators to the same setting. More recently, (Zhao et al., 2025) provide asymptotic convergence guarantees for separable drift estimation in a compact domain using feed-forward neural networks. Their empirical evaluation, however, is restricted to a single test drift function and assesses recovery only along one coordinate of a high-dimensional system, leaving performance on fully coupled dynamics unexamined.

2.2. Score-based generative models

Score-based generative models, or *Denoising Diffusion Models (DDMs)*, were introduced in (Ho et al., 2020) and (Song et al., 2021b), drawing ideas from score-matching (Hyvarinen & Dayan, 2005; Vincent, 2011) and building on earlier work (Sohl-Dickstein et al., 2015). By using neural networks to estimate the log density of a smoothed data distribution, i.e. the *score*, they have achieved state-of-the-art results in image generation (Ho et al., 2020; Dhariwal & Nichol, 2021; Saharia et al., 2022; Brooks et al., 2023), and have found numerous applications in video generation (Ho et al., 2022), molecule and drug design, (Xu et al., 2023; Corso et al., 2023), strategy testing (Koshiyama et al., 2021), and data sharing (Assefa, 2020).

Their state-of-the-art performance across several domains, and the fact that they are less susceptible to training instabilities or mode-collapse, have established DDMs as the gold-standard in generative modelling (Dhariwal & Nichol, 2021). In particular, (Song & Ermon, 2019) extended (Sohl-Dickstein et al., 2015) to a practical setting by formalising Stochastic Gradient Langevin Dynamics (SGLD) as the latent variable process, while (Ho et al., 2020) introduced Denoising Diffusion Probabilistic Models (DDPM). These approaches were unified under an SDE-based framework in (Song et al., 2021c), who show that the forward processes in DDPM and SGLD are discretisations of continuous-time Itô-SDEs. Further generalisations

have been achieved in recent years, see (Song et al., 2021a; Franzese et al., 2023; Zhang et al., 2023; Benton et al., 2024). Other contributions have proposed improvements to accelerate sampling or to improve sample quality, such as (Jolicœur-Martineau et al., 2021; Bao et al., 2022; Watson et al., 2022; Xu et al., 2022; Rombach et al., 2022). Finally, using ideas from optimal transport, (De Bortoli et al., 2021; Shi et al., 2022; 2023) developed a parallel line of work, connecting diffusion models to Schrödinger bridge problems.

2.2.1. LEARNING THE SCORE FOR TIME SERIES DATA

Beyond image and spatial data, score-based diffusion models have also been extensively applied to time-series settings, see (Lin et al., 2023) for a comprehensive survey. While the methods reviewed below are not used directly in this work, they illustrate how diffusion models have been adapted to temporal and conditional structures, and therefore provide relevant context for our setting.

In the field of time series forecasting, (Lim et al., 2023) draw inspiration from the TimeGrad model in (Rasul et al., 2021; Kong et al., 2021) and the ScoreGrad model in (Yan et al., 2021) to propose the TSGM model, a conditional diffusion model that operates on a low-dimensional representation of the data. (Shen & Kwok, 2023) remove the sequence-based architecture (LSTM, Transformer) to achieve non-autoregressive forecasting. For time-series with missing values, (Taskhiro et al., 2021; Alcaraz & Strodthoff, 2023; Kolloviev et al., 2023) proposed conditional diffusion frameworks that impute unobserved entries. For long-horizon multivariate sequence generation, (Barancikova et al., 2025) introduce SigDiffusion, which leverages path signatures. In the domain of filtering, (Bao et al., 2022; 2024) applied score-based conditional diffusion models to non-linear filtering problems.

3. Background

3.1. Score-based diffusion models

Score-based diffusion models are generative models that learn a reversible transformation between two distributions, p_0 and p_1 . (Song et al., 2021b) used a forward SDE to transform samples distributed according to p_0 to samples distributed according to p_1 . Defining $\gamma(\tau) = \gamma_0 + \tau(\gamma_1 - \gamma_0)$, the forward SDE takes samples $X_0 \sim p_0$ and diffuses them towards $X_1 \sim p_1$ via a Variance-Preserving SDE (VPSDE),

$$dX_\tau = -\frac{1}{2}\gamma(\tau)X_\tau d\tau + \sqrt{\gamma(\tau)}dW_\tau, \quad \tau \in [0, 1], \quad (6)$$

where $(W_\tau)_{\tau \in [0,1]}$ is a D -dimensional Brownian motion, see Section 3.4 in (Song et al., 2021b). We emphasise (6) is a different SDE to the data-generating process assumed in

(1), and which defines the distribution p_0 . From (Anderson, 1982), the forward SDE in (6) admits a time-reversal which diffuses $\tilde{X}_0 \sim p_1$ back to $\tilde{X}_1 \sim p_0$ via,

$$d\tilde{X}_\tau = \left[\frac{1}{2}\tilde{X}_\tau + \nabla_{\tilde{X}_\tau} \ln p_\tau(\tilde{X}_\tau) \right] \gamma(\tau) d\tau + \sqrt{\gamma(\tau)} d\tilde{W}_\tau, \quad (7)$$

such that $\tilde{X}_\tau \stackrel{d}{=} X_{1-\tau}$, $\tilde{W}_\tau \stackrel{d}{=} W_{1-\tau} \forall \tau \in [0, 1]$, where $\stackrel{d}{=}$ means equal in distribution.

The reverse-time SDE in (7) requires access to the score $\nabla_{X_\tau} \ln p_\tau(X_\tau)$ which is not available in closed form in general. (Vincent, 2011; Song et al., 2021b) show that the oracle score-matching objective is,

$$l(\theta) = \int_0^1 \mathbb{E} \left[\lambda(\tau) \|s_\theta(\tau, X_\tau) - \nabla_{X_\tau} \ln p_\tau(X_\tau)\|_2^2 \right] d\tau,$$

where $X_0 \sim p_0(x_0)$, $X_\tau \sim q_\tau(x_\tau | X_0)$ and $s_\theta : [0, 1] \times \mathbb{R}^D \rightarrow \mathbb{R}^D$ is a neural network parameterised by θ . The function $\lambda : [0, 1] \rightarrow \mathbb{R}^+$ is a positive weighting function, and $q_\tau(x_\tau | X_0)$ is the transition density of (6),

$$q_\tau(x_\tau | X_0) = \mathcal{N}(x_\tau; \beta_\tau X_0, \sigma_\tau^2 I), \quad (8)$$

where we have defined $\sigma_\tau^2 = 1 - \beta_\tau^2$ and $\beta_\tau = \exp[-0.25\tau^2(\gamma_1 - \gamma_0) - 0.5\tau\gamma_0]$.

However, the objective $l(\theta)$ cannot be evaluated in practice since we do not have access to the score. Under sufficient expressivity of the neural network s_θ , (Vincent, 2011) show that the denoising score-matching objective has the same global minimum as $l(\theta)$,

$$\tilde{l}(\theta) = \int_0^1 \mathbb{E} \left[\lambda(\tau) \|s_\theta(\tau, X_\tau) - \nabla_{X_\tau} \ln q_\tau(X_\tau | X_0)\|_2^2 \right] d\tau.$$

(Song & Ermon, 2019), (Song et al., 2021b) proposed the weighting function $\lambda(\tau) = \sigma_\tau^2$ to reduce the variance of the target $\nabla_{X_\tau} \ln q_\tau(X_\tau | X_0) = -\sigma_\tau^{-2}(X_\tau - \beta_\tau X_0)$. In practice, the objective $\tilde{l}(\theta)$ is approximated via Monte Carlo sampling. In particular, one samples $(\tau, X_0) \sim \mathcal{U}[\epsilon, 1] \times p_0$ and then $X_\tau \sim q_\tau(x_\tau | X_0)$ for each sample. The constant $\epsilon > 0$ is chosen to avoid the explosion of the target since $\lim_{\tau \rightarrow 0} \sigma_\tau = 0$.

3.2. Conditional diffusion models

Letting $(X_0, Y) \sim p_0(x_0, y)$, $Y \in \mathbb{R}^D$, (Song et al., 2021b), (Taskhiro et al., 2021) apply score-based diffusion models to generate samples from $p_0(x_0 | Y)$. For each fixed Y , applying the forward diffusion (6) to X_0 induces a push-forward distribution $p_\tau(x_\tau | Y) \forall \tau \in [0, 1]$. Similar to (7), the reverse-time SDE for conditional generation is:

$$d\tilde{X}_\tau = \left[\frac{1}{2}\tilde{X}_\tau + \nabla_{\tilde{X}_\tau} \ln p_\tau(\tilde{X}_\tau | Y) \right] \gamma(\tau) d\tau + \sqrt{\gamma(\tau)} d\tilde{W}_\tau. \quad (9)$$

(Theorem 1, Appendices B.1-B.2) (Batzolis et al., 2021) show one can learn the conditional score in (9) consistently by minimising the following objective,

$$\tilde{L}(\theta) = \mathbb{E} \left[\lambda(\tau) \left\| s_\theta(\tau, X_\tau, Y) - \nabla_{X_\tau} \ln q_\tau(X_\tau | X_0) \right\|_2^2 \right], \quad (10)$$

The conditional score can be written in terms of the denoiser,

$$\nabla_{X_\tau} \ln p_\tau(X_\tau | Y) = -\frac{X_\tau}{\sigma_\tau^2} + \frac{\beta_\tau}{\sigma_\tau^2} \mathbb{E}[X_0 | X_\tau, Y], \quad (11)$$

where the denoiser is given by,

$$\mathbb{E}[X_0 | X_\tau, Y] = \int_{\mathbb{R}^D} x_0 p(x_0 | X_\tau, Y) dx_0. \quad (12)$$

To learn the denoiser directly, one can re-parameterise s_θ using a network D_θ ,

$$s_\theta(\tau, X_\tau, Y) = -\frac{X_\tau}{\sigma_\tau^2} + \frac{\beta_\tau}{\sigma_\tau^2} D_\theta(\tau, X_\tau, Y) \quad (13)$$

which can be plugged into the learning objective (10) for s_θ to yield a learning objective for D_θ ,

$$\tilde{L}(\theta) = \mathbb{E} \left[\left\| D_\theta(\tau, X_\tau, Y) - X_0 \right\|_2^2 \right]. \quad (14)$$

4. Estimation of the drift function

In this section, we study how to recover the drift $\mu(Y)$ from a denoising model trained to approximate the denoiser $\mathbb{E}[X_0 | X_\tau, Y]$. We exploit the Gaussian structure of the forward process to construct a Monte Carlo estimator for μ .

4.1. Data specification for conditional diffusion models

Given trajectories $Y^{(i)}$ observed at times $t_j = j\Delta$, recall we define $\forall j \in \{0, \dots, J-1\}$ the increment,

$$Z_{t_j}^{(i)} := Y_{t_{j+1}}^{(i)} - Y_{t_j}^{(i)}.$$

From (2), $Z_{t_j}^{(i)}$ depends on the past trajectory $(Y_{t_s}^{(i)})_{s=0}^j$ only through the current observation $Y_{t_j}^{(i)}$. Consequently, under the time-homogeneous dynamics in (1), the conditional law of $Z_{t_j}^{(i)}$ given $Y_{t_j}^{(i)}$ is independent of j , and we work with generic pairs (Y, Z) , suppressing the indices i and j .

Henceforth, X_0 will denote an increment from the data generating distribution $p_0(x_0 | Y)$, and X_τ is the diffused version of X_0 after applying the forward process q_τ in (8). We aim to learn an approximation $D_\theta(\tau, X_\tau, Y)$ to the denoising target $\mathbb{E}[X_0 | X_\tau, Y]$ by minimising (10).

4.2. Learning the drift by denoising

We suppose henceforth that θ^* is the minimiser of (14) such that $D_{\theta^*}(\tau, X_\tau, Y)$ is the trained approximation to $\mathbb{E}[X_0 | X_\tau, Y]$. We also use the Euler-Maruyama approximation to the increment distribution in (4), $p_0(x_0 | Y) \approx \hat{p}_0(x_0 | Y) = \mathcal{N}(x_0; \mu(Y)\Delta, \Delta)$ to derive an estimator for μ .

Under the VPSDE, the transition kernel $q_\tau(x_\tau | X_0)$ in (8) is a Gaussian linear in X_0 . Since the conditional distribution $\hat{p}_0(x_0 | Y)$ is also Gaussian, a closed-form solution for the denoiser is obtained under the EM approximation,

$$\mathbb{E}[X_0 | X_\tau, Y] \approx \frac{\sigma_\tau^2 \Delta}{\sigma_\tau^2 + \beta_\tau^2 \Delta} \left[\mu(Y) + \frac{\beta_\tau}{\sigma_\tau^2} X_\tau \right],$$

and the drift is obtained through,

$$\mu(Y) = a(\tau)X_\tau + b_\Delta(\tau)\mathbb{E}[X_0 | X_\tau, Y], \quad (15)$$

where,

$$a(\tau) := -\frac{\beta_\tau}{\sigma_\tau^2}, \quad b_\Delta(\tau) := \frac{\sigma_\tau^2 + \beta_\tau^2 \Delta}{\sigma_\tau^2 \Delta}. \quad (16)$$

For a given $Y = y$, let $x_\tau^{(k)} \sim p_\tau(x_\tau | y) \forall k \in [\mathcal{K}]$. We can construct a single-sample estimator,

$$\hat{\mu}(\tau, x_\tau^{(k)}, y) = a(\tau)x_\tau^{(k)} + b_\Delta(\tau)D_{\theta^*}(\tau, x_\tau^{(k)}, y), \quad (17)$$

where $x_\tau^{(k)}$ enters as a linear correction to the learned denoiser, constructed in a way that preserves unbiasedness in the ideal case of (15). By averaging over the \mathcal{K} samples $x_\tau^{(k)}$, we can estimate the drift with,

$$\bar{\mu}(\tau, y) = \frac{1}{\mathcal{K}} \sum_{k \in [\mathcal{K}]} \hat{\mu}(\tau, x_\tau^{(k)}, y). \quad (18)$$

For sufficiently large \mathcal{K} , the estimator $\bar{\mu}(\tau, y)$ removes the linear dependence of the rescaled denoiser on X_τ in (15), and can be cast as a lower-variance alternative to $\hat{\mu}(\tau, x_\tau^{(k)}, y)$.

We emphasise that the Euler-Maruyama approximation used to derive (18) is not imposed during training, but only at the stage of drift estimation.

4.3. Choice of diffusion time for drift estimator

To implement the estimator in (18), a value of $\tau \in [0, 1]$ must be chosen, and \mathcal{K} samples $x_\tau^{(k)} \sim p_\tau(x_\tau | Y = y)$ must be drawn. One expects there to exist an intermediate noise level $0 < \tau < 1$ for which the denoising problem is well conditioned and the drift approximation error in $\bar{\mu}$ is low.

We propose setting $\tau = 1$ as a convenient and empirically robust choice, as motivated in the remainder of this section. At $\tau = 1$, one should first sample \mathcal{K} standard normal

random variables $x_1^{(k)} \sim \mathcal{N}(0, I)$. The drift in (17) is then,

$$\widehat{\mu}(1, x_1^{(k)}, y) = a(1)x_1^{(k)} + b_\Delta(1)D_{\theta^*}(1, x_1^{(k)}, y),$$

Averaging over all \mathcal{K} samples yields $\bar{\mu}(y) := \bar{\mu}(1, y)$,

$$\bar{\mu}(y) = \frac{1}{\mathcal{K}} \sum_{k \in [\mathcal{K}]} \widehat{\mu}(1, x_1^{(k)}, y). \quad (19)$$

To justify why $\tau = 1$ is appropriate, we empirically investigate the dependence of the estimator $\bar{\mu}(\tau, y)$ on τ . In principle, samples $x_\tau^{(k)} \sim p_\tau(x_\tau | y)$ can be drawn by sampling $(x_0, y) \sim p_0(x_0, y)$ from the dataset \mathcal{D} and applying the forward process q_τ in (8). However, this approach is limited to values of y observed in the dataset and scales poorly with dimension. Therefore, sampling $x_\tau^{(k)}$ from $p_\tau(x_\tau | y)$ for different values of τ is implemented by simulating the reverse diffusion (9), see (Song et al., 2021b; Karras et al., 2022), for details on different numerical implementations. The VPSDE forward process in (8) ensures $X_\tau \simeq \mathcal{N}(0, I)$ for large τ . We can therefore sample $x_1^{(k)} \sim \mathcal{N}(0, I)$ and run the reverse diffusion in (9) to obtain approximate samples from $p_\tau(x_\tau | y)$ for intermediate diffusion times.

During validation, we set $\mathcal{K} = 10$ and allow oracle access to the true drift to select the model which minimises the τ -averaged drift mean-squared error (MSE),

$$\hat{\theta} = \arg \min_{\theta} \mathbb{E}_\tau \mathbb{E} \left[\|\bar{\mu}(\tau, Y) - \mu(Y)\|_2^2 \right],$$

We choose to test this approach using two representative drift functions,

$$\mu^{(1)}(y) = -y + \sin(25y), \quad y \in \mathbb{R} \quad (20)$$

$$\mu_d^{(2)}(y) = -4a_d y_d^3 - 2b_d y_d, \quad y \in \mathbb{R}^D, \quad d \in [D] \quad (21)$$

where $a_d > 0, b_d < 0 \forall d \in [D]$. Given a set of N points uniformly spaced $y_n \in \mathcal{R} \subset \mathbb{R}^D$, we approximate the drift MSE as,

$$e^2(\tau) \approx \frac{1}{N} \sum_{n \in [N]} \|\mu(y_n) - \bar{\mu}(\tau, y_n)\|_2^2. \quad (22)$$

Figure 1 shows the error $e^2(\tau)$ when estimating $\mu^{(1)}$ for $\mathcal{K} \in \{1, 10, 100\}$. In all cases, the drift MSE diverges as $\tau \rightarrow 0$, as the approximation error in the network D_{θ^*} is expected to increase for smaller τ (Song et al., 2021b). The error is minimised for $\tau \approx 0.2$, but as \mathcal{K} increases, the error curve becomes flat and less sensitive to τ , and larger values yield similar performance. Indeed, the bottom two panels in Figure 1 demonstrate accurate recovery of $\mu^{(1)}$ for $\tau \in \{0.2, 1\}$ when $\mathcal{K} = 100$.

Similarly, Figure 2 illustrates the drift error $e^2(\tau)$ when estimating $\mu^{(2)}$ for $D = 8$ (top row) and $D = 12$ (bottom row), exhibiting behaviour similar to Figure 1 even in

higher dimensions.

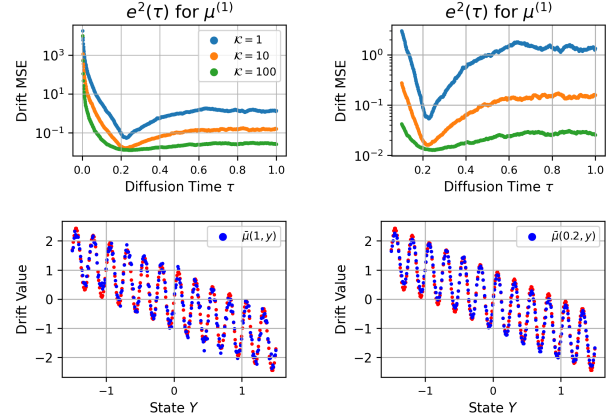


Figure 1. The top-left panel shows the drift error $e^2(\tau)$ when estimating $\mu^{(1)}$; the top-right panel restricts the range of τ to $\tau \in [0.15, 1]$. The bottom row compares the true drift with $\bar{\mu}(\tau, y)$ for $\tau = 1$ (left) and optimal $\tau \approx 0.2$ (right) for $\mathcal{K} = 100$. Positions Y are uniformly spaced between $[-1.5, 1.5]$, covering 99% of the training distribution.

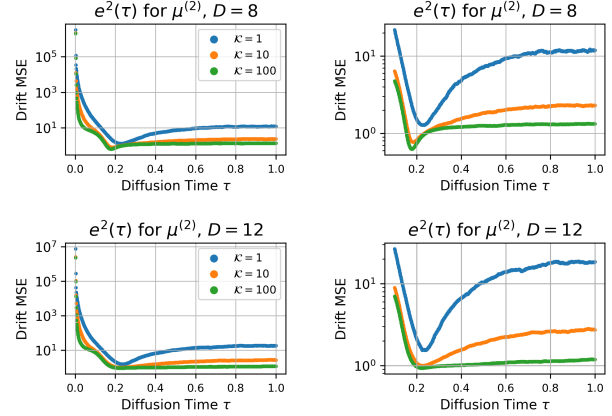


Figure 2. The left panels show the drift error $e^2(\tau) \forall \tau \in [0, 1]$; the right panels restrict the range of τ to $\tau \in [0.15, 1]$. The top row shows the drift error $e^2(\tau)$ $\mu^{(2)}$ with $D = 8$; the bottom row shows the same for $D = 12$.

We emphasise here that there is no closed form solution to selecting the optimal τ since the approximation error in D_{θ^*} is architecture and data dependent. Further, the choice of forward noise schedule will impact the dependence of the estimator on τ , see Appendix A for a comparison with the Variance Exploding SDE. Therefore, there is no guarantee that a specific τ is optimal across architectures and noise schedules. Moreover, the computational cost of simulating the reverse diffusion process is high. In contrast, sampling from the approximate terminal distribution $X_1 \sim \mathcal{N}(0, I)$ is cheap, and for large \mathcal{K} , the error at $\tau = 1$ is similar to the optimal error. As such, we suggest using $\tau = 1$ to implement our estimator (19), and the results in Section 5.4 confirm that even with this choice of τ , we achieve competitive performance.

5. Experiments

5.1. Evaluation Criterion

We evaluate the performance of a drift estimator $\tilde{\mu}$ using the time-integrated mean-squared error,

$$E_t^{(\mu)} = \frac{1}{t} \int_0^t \mathbb{E} \|\tilde{\mu}(Y_s) - \mu(Y_s)\|_2^2 ds \quad (23)$$

where the expectation is over the law of the process $(Y_s)_s$.

In practice, we approximate (23) in the following way. Let $\{Y^{(i)}\}_i, i \in [\mathcal{I}]$ be a set of i.i.d trajectories from (1) with \mathcal{J} discrete observations. We approximate (23) using $\forall j \in [\mathcal{J}]$,

$$E_{j\Delta}^{(\mu)} := \frac{1}{j\mathcal{I}} \sum_{i \in [\mathcal{I}]} \sum_{k \in [j]} \left\| \tilde{\mu}(Y_{t_k}^{(i)}) - \mu(Y_{t_k}^{(i)}) \right\|_2^2,$$

where \mathcal{I}, \mathcal{J} denote the number of trajectories and observations, respectively, used for error evaluation. In contrast, I, J denote the number of training trajectories and observations, respectively.

5.2. Implementation

In all experiments, training datasets consist of $I = 10^3$ sample paths generated from an Euler discretisation of (1) with $\sigma = 1$ for $t \in [0, 1]$ at a frequency of $\Delta = 256^{-1}$. All drift estimators are fitted with fixed random seeds for reproducibility. In-sample errors are computed by simulating $\mathcal{I} = 10^3$ new trajectories over the in-sample horizon $t \in [0, 1]$ with $\Delta = 256^{-1}$, while out-of-sample errors are computed over $t \in [0, 20]$. We will denote by DN the denoising estimator $\tilde{\mu}$ in (19) which uses the trained network D_{θ^*} , see Appendix B for architectural details.

For one dimensional drift functions, we compare DN against three nonparametric estimators used in drift estimation under i.i.d trajectories. Specifically, we implement the IID Nadaraya–Watson estimator (Marie & Rosier, 2023), a kernel-based estimator obtained by averaging increments across independent trajectories; the IID Ridge (Denis et al., 2021), a spline-based least-squares estimator using B-spline bases with ridge regularization, and the IID Hermite projection (Comte & Genon-Catalot, 2020), which estimates the drift via least-squares projection onto a finite-dimensional Hermite basis, see Appendix C for more details.

In higher dimensions, the computational and data requirements of the Ridge and Hermite estimators of (Denis et al., 2021) and (Comte & Genon-Catalot, 2020) grow exponentially with D (Zhao et al., 2025), and kernel-based estimators such as the Nadaraya Watson deteriorate rapidly, as seen in Appendix E. We therefore omit them from the main text when estimating high dimensional drift functions.

To benchmark DN in high dimensions, we implement the proposed estimator in (Zhao et al., 2025), and refer to it as FC. The estimator FC is the output of a feed-forward ReLU network trained to regress the scaled increments $\Delta^{-1}X_0$ from the states Y using (5), corresponding to a standard regression objective, without any denoising mechanism. We follow (Zhao et al., 2025) in imposing sparsity and weight-clamping constraints on the network parameters during training. These constraints restrict the hypothesis class to separable drifts and are part of the estimator definition in (Zhao et al., 2025). For consistency, all neural-network based estimators are trained to target $\Delta^{-1}X_0$.

Our denoising network D_{θ^*} includes a learnable embedding applied to states Y , referred to as *MLPStateMapper*, which combines polynomial and Fourier features and feeds into the remaining network. It also includes a parallel one-dimensional convolutional module to capture local spatial structure in (Y, X_τ) , see Appendix B for more details. As the performance of DN depends on both denoising-based training and architectural inductive biases in D_{θ^*} , we introduce three control baselines to attempt to disentangle their contributions.

We denote by FC^+ the FC estimator with its parameter count matched to D_{θ^*} , and remove the sparsity and weight-clamping restrictions in (Zhao et al., 2025). We further introduce FC^+ -Conv, which augments the fully connected layers with a similar parallel convolutional module as D_{θ^*} . Both FC^+ , FC^+ -Conv are trained on the same objective as FC, i.e., the standard regression objective. Therefore, estimators FC^+ , FC^+ -Conv help to isolate the effect of denoising by controlling for differences in model capacity and inductive bias. Finally, we define DN-Lin as a variant of DN in which the *MLPStateMapper* in D_{θ^*} is replaced by a fully connected mapping, helping to isolate the effect of learned state embeddings in drift estimation.

All estimators are selected by minimising the oracle error $E_{j\Delta}^{(\mu)}$ at the in-sample terminal time $j\Delta = 1$. For the one-dimensional benchmarks, hyperparameters are chosen via grid search, see Appendix D. For neural network based estimators, (FC, FC^+ , FC^+ -Conv, DN-Lin and DN), we evaluate the error $E_1^{(\mu)}$ on $\mathcal{I} = 50$ held-out trajectories at every epoch and terminate training when $E_1^{(\mu)}$ has not improved over 100 epochs, see Appendix D for more details. Sensitivity to reduced training dataset size and to sampling frequency Δ are explored in Appendix F and H, respectively, and Appendix I provides a performance comparison when we use a feasible model selection objective for DN, DN-Lin.

5.3. Test Drift Functions

For $D = 1$, we consider the following one-dimensional drift functions,

$$\begin{aligned}\mu_1(y) &= -\sin(2y) \log(1 + 5|y|), \\ \mu_2(y) &= -y + \sin(25y), \\ \mu_3(y) &= -y^3 + y.\end{aligned}$$

To consider high-dimensional drifts derived from scalar potentials, we use the following parametric family,

$$\begin{aligned}\mu_{4,d}(y) &= -4a_d y_d^3 - 2b_d y_d \\ &\quad - \frac{c}{2} \psi'_d(y_d) [\psi_{d-1}(y_{d-1}) + \psi_{d+1}(y_{d+1})],\end{aligned}$$

where the coefficients satisfy $a_d > 0, b_d < 0$, and c is a coupling constant. For $c = 0$, μ_4 collapses to a separable bi-stable potential with wells at $y_{*,d} = \pm \sqrt{-\frac{b_d}{2a_d}}$. For $c > 0$, coordinate interaction is introduced via $\psi_d(y_d) = \exp(-\frac{(y_d - y_{*,d})^2}{2s_d^2})$, and $s_d = \sqrt{c} y_{*,d}$.

To consider non-potential and chaotic dynamics, we use the following drift, $\forall d \in \{0, \dots, D-1\}$ and $F > 0$,

$$\mu_{5,d}(y) = (y_{d+1} - y_{d-2})y_{d-1} - y_d + F,$$

where indices are taken modulo D . For $F < 1$, μ_5 defines the Lorenz-96 system which exhibits stable behaviour, whereas chaotic behaviour emerges for standard choices such as $F = 8$ (Lorenz, 1996).

5.4. Results

5.4.1. IN SAMPLE RESULTS

Table 1 reports final-time in-sample errors $E_1^{(\mu)}$ for the one-dimensional benchmarks. The denoising-based estimator attains errors of the same order of magnitude as classical nonparametric methods, and Figure 3 illustrates that it accurately recovers the structure of the drift.

Table 1. In-sample drift errors $E_1^{(\mu)}$, for μ_1, μ_2, μ_3 . Best estimator is starred, second-best is underlined.

$E_1^{(\mu)}$	DN	NW	Hermite	Ridge
μ_1	<u>0.02127</u>	0.04564	0.007621*	0.02382
μ_2	0.01870*	0.1320	0.5049	<u>0.0574</u>
μ_3	<u>0.00754</u>	0.01464	0.005082*	0.1739

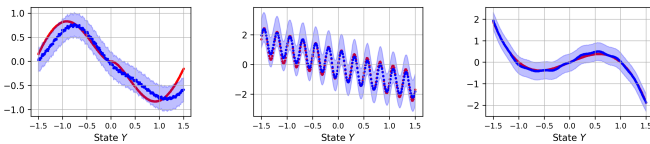


Figure 3. Panels (left to right) correspond to μ_1, μ_2, μ_3 . True drift against DN drift. Shaded region shows 10 – 90% quantile envelope over \mathcal{K} . State values cover 99% of the training distribution.

In higher dimensions, Table 2 shows that the denoising estimator DN achieves the lowest in-sample error when estimating the bistable drift μ_4 across both separable ($c = 0$) and strongly coupled ($c = 20$) regimes. In the separable case, (DN-Lin) performs poorly in relation to DN, suggesting that denoising-based drift estimation depends on an inductive bias aligned with the drift structure in order to accurately learn the drift over the in-sample distribution.

Table 2. In-sample drift errors $E_1^{(\mu)}$, for μ_4 . Best estimator is starred, second-best is underlined.

c	D	DN	DN-Lin	FC ⁺ -Conv	FC ⁺	FC
0	8	1.047*	6.941	<u>3.898</u>	8.865	7.687
	12	1.681*	11.294	<u>6.316</u>	14.276	14.157
20	8	8.490*	10.335	<u>9.048</u>	16.287	35.365
	12	10.660*	<u>13.648</u>	14.076	29.528	46.166

Figure 4 overlays the true and estimated drift DN for selected dimensions of μ_4 , illustrating accurate recovery in intermediate dimensions and expected degradation in the highest-index dimension.

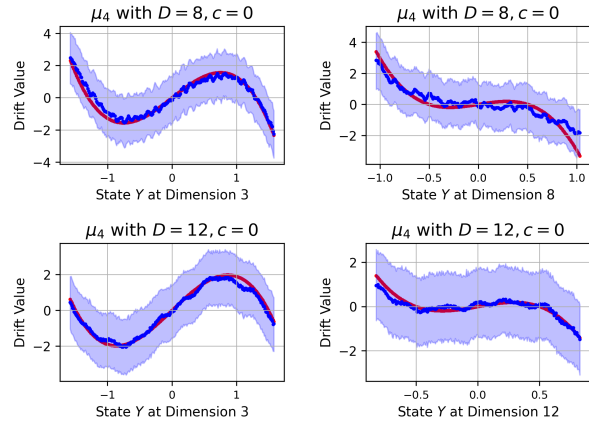


Figure 4. True drift against the DN drift for $\mu_4, c = 0$. State values cover 99% of the training distribution in each dimension. Top panels show dimensions 3 (left) and 8 (right) for $D = 8$. Bottom panels show dimensions 3 (left) and 12 (right) for $D = 12$. Shaded region denotes 10 – 90% quantile envelope over \mathcal{K} .

Table 3 reports in-sample results for the Lorenz 96 drift μ_5 . Performance is dominated by architectural inductive bias, as estimators with convolutional architectures (DN, DN-Lin, FC⁺-Conv) achieve similar accuracy while fully connected baselines perform poorly.

Table 3. In-sample drift errors $E_1^{(\mu)}$, for μ_5 .

F	D	DN	DN-Lin	FC ⁺ -Conv	FC ⁺	FC
$\frac{1}{2}$	20	4.870	3.127*	<u>3.733</u>	18.554	49.862
	40	<u>9.596</u>	7.766*	11.940	44.764	62.988
8	20	<u>9.542</u>	5.725*	11.486	127.103	926.707
	40	17.898	12.203*	<u>16.306</u>	1263.290	2583.505

Overall, the results indicate that denoising-based estimators yield the strongest in-sample performance when paired with a network whose inductive bias is aligned with the underlying dynamics. However, since all networks are selected by oracle in-sample error during training, these results reflect best-case fitting and may not be indicative of the relative generalisation behaviour of denoising and standard regression estimators.

5.4.2. OUT OF SAMPLE RESULTS

We evaluate out-of-sample (OOS) performance by simulating trajectories beyond the training horizon, where the system in (1) evolves into regions of state space not observed during training.

Table 4 reports final-time OOS errors for the bistable drift μ_4 . In the non-separable regime ($c = 20$), the denoising estimators (DN, DN-Lin) achieve the lowest OOS error compared to all standard regression baselines across dimensions. Figure 5 shows that the OOS error of DN grows more slowly over time, leading to increasing separation from FC⁺-Conv. This advantage persists even when the FC⁺-Conv baseline is augmented with the *MLPStateMapper* state embedding (see Appendix G), suggesting that the performance gap of DN is not explained by architecture alone.

Table 4. Final-time OOS drift errors $E_{20}^{(\mu)}$, for μ_4 .

c	D	DN	DN-Lin	FC ⁺ -Conv	FC ⁺	FC
0	8	1.546*	11.800	<u>9.744</u>	14.129	14.365
	12	2.314*	16.616	<u>8.344</u>	21.523	23.658
20	8	50.919*	<u>67.297</u>	76.061	70.134	67.299
	12	81.721*	<u>115.750</u>	121.379	182.499	105.854

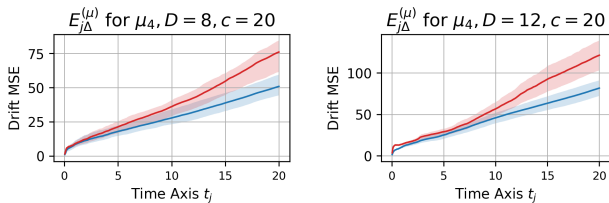


Figure 5. OOS $E_{j\Delta}^{(\mu)}$ for μ_4 , $c = 20$, for DN, and FC⁺-Conv. Shaded region shows 10 – 90% quantile envelope over test trajectories \mathcal{I} .

Table 5 reports OOS results for the Lorenz 96 drift μ_5 . In the stable regime ($F = 0.5$), the estimators with convolutional networks achieve comparable OOS performance. In the chaotic regime ($F = 8$), the denoising-based estimator DN-Lin consistently attains lower OOS error than FC⁺-Conv across dimensions. Since both estimators share the same inductive bias, these results suggest a generalisation benefit attributable to the denoising training objective rather than architectural differences. The denoising variant DN underperforms in this setting, reflecting misalignment

of the *MLPStateMapper* state embedding with the Lorenz 96 dynamics. Figure 6 shows that while OOS errors stabilise over time, DN-Lin plateaus at a lower error level than standard regression.

Table 5. Final-time OOS drift error $E_{20}^{(\mu)}$, for μ_5 .

F	D	DN	DN-Lin	FC ⁺ -Conv	FC ⁺	FC
$\frac{1}{2}$	20	8.718	12.024	7.920*	44.376	56.041
	40	<u>12.198</u>	11.134*	12.802	99.322	167.826
8	20	3973	172.786*	<u>226.361</u>	7457	8425
	40	1243	332.905*	<u>527.726</u>	16280	17656

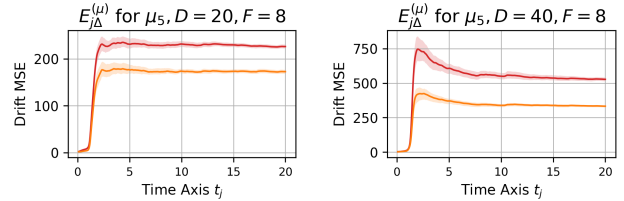


Figure 6. OOS $E_{j\Delta}^{(\mu)}$ for μ_5 , $F = 8$ comparing the DN-Lin, FC⁺-Conv estimators. Shaded region shows 10 – 90% quantile envelope across test trajectories \mathcal{I} .

Taken together, the OOS results for μ_4 and μ_5 suggest standard regression, when paired with an architecture aligned the underlying drift, can achieve strong in-sample performance, yet may generalise poorly out of sample in strongly coupled or chaotic dynamics. In these settings, the denoising estimator with an appropriate architecture provides improved generalisation, while remaining competitive when networks trained via standard regression already generalise well.

6. Conclusion

This paper adapts score-based conditional diffusion models to the problem of high-dimensional drift estimation from discretely observed trajectories. By introducing controlled Gaussian corruption to the observed increments, we train a neural network to learn the denoiser of each increment conditional on the previous state. Using the trained network, we derived an estimator for the drift through a first-order approximation of the data-generating process. Across a range of drift structures and dimensions, our results show that denoising can complement architectural inductive bias to improve out-of-sample robustness in settings with strong interactions or chaotic dynamics. In contrast, when standard regression already generalises stably out of sample, denoising can remain competitive. Several important questions remain open. These include developing a theoretical understanding for how different noise schedules affect the bias-variance properties of the estimator under specific architectures, as well as extending the estimator construction to incorporate higher order approximations of the denoising target.

7. Impact Statement

This paper presents work whose goal is to advance the field of Machine Learning. There are many potential societal consequences of our work, none which we feel must be specifically highlighted here.

References

- Ait-Sahalia, Y. Maximum likelihood estimation of discretely sampled diffusions: A closed-form approximation approach. *Econometrica*, 70(1):223–262, 2002.
- Alcaraz, J. M. L. and Strodthoff, N. Diffusion-based conditional ecg generation with structured state space models, 2023.
- Anderson, B. D. O. Reverse-time diffusion equation models. *Stochastic Processes and their Applications*, 12(3): 313–326, 1982. doi: 10.1016/0304-4149(82)90051-5.
- Assefa, S. *Generating Synthetic Data in Finance: Opportunities, Challenges and Pitfalls*. SSRN, 2020. URL <http://dx.doi.org/10.2139/ssrn.3634235>.
- Bandi, F. M. and Phillips, P. C. B. Fully nonparametric estimation of scalar diffusion models. *Econometrica*, 71(1):241–283, 2003.
- Bandi, F. M. and Phillips, P. C. B. A simple approach to the parametric estimation of diffusion processes. *Journal of Econometrics*, 141(1):62–94, 2007.
- Bao, F., Li, C., Zhu, J., and Zhang, B. Analytic-DPM: an analytic estimate of the optimal reverse variance in diffusion probabilistic models. In *International Conference on Learning Representations*, 2022. URL <https://openreview.net/forum?id=0xiJLKH-ufZ>.
- Bao, F., Zhang, Z., and Zhang, G. A score-based filter for nonlinear data assimilation. *Journal of Computational Physics*, 514:113207, Oct 2024. ISSN 0021-9991. doi: 10.1016/j.jcp.2024.113207.
- Barancikova, B., Huang, Z., and Salvi, C. Sigdiffusions: Score-based diffusion models for time series via log-signature embeddings. In *International Conference on Learning Representations (ICLR) 2025*, 2025. URL <https://openreview.net/forum?id=Y8KK9kjgIK>.
- Barndorff-Nielsen, O. E. and Shephard, N. Econometric analysis of realized volatility and its use in estimating stochastic volatility models. *Journal of the Royal Statistical Society: Series B*, 64(2):253–280, 2002.
- Batzolis, G., Stanczuk, J., Schönlieb, C.-B., and Etmann, C. Conditional image generation with score-based diffusion models. In *Advances in Neural Information Processing Systems*, volume 34, 2021.
- Benton, J., Shi, Y., De Bortoli, V., Deligiannidis, G., and Doucet, A. From denoising diffusions to denoising markov models. *Journal of the Royal Statistical Society, Series B: Statistical Methodology*, 86(2):286–301, Apr 2024. doi: 10.1093/jrssi/bqkae005.
- Bishop, C. M. Training with noise is equivalent to tikhonov regularization. *Neural Computation*, 7(1):108–116, 1995. doi: 10.1162/neco.1995.7.1.108.
- Bonalli, R. and Rudi, A. Non-parametric Learning of Stochastic Differential Equations with Non-asymptotic Fast Rates of Convergence. *Foundations of Computational Mathematics*, 25(3), mar 2025. doi: 10.1007/s10208-025-09705-x.
- Brooks, T., Holynski, A., and Efros, A. A. Instructpix2pix: Learning to follow image editing instructions. In *Proceedings of the IEEE/CVF Conference on Computer Vision and Pattern Recognition (CVPR)*, pp. 19530–19539, 2023. doi: 10.1109/CVPR52688.2023.01908.
- Comte, F. and Genon-Catalot, V. Nonparametric drift estimation for diffusion processes. *Stochastic Processes and their Applications*, 119(12):4088–4123, 2009.
- Comte, F. and Genon-Catalot, V. Adaptive estimation of the drift function for ergodic diffusions: A penalized projection approach. *Bernoulli*, 16(3):617–652, 2010.
- Comte, F. and Genon-Catalot, V. Nonparametric drift estimation for i.i.d. paths of stochastic differential equations. *The Annals of Statistics*, 48(6):3336–3365, 2020. doi: 10.1214/19-AOS1933. URL <https://doi.org/10.1214/19-AOS1933>.
- Corso, G., Stärk, H., Jing, B., Barzilay, R., and Jaakkola, T. Diffdock: Diffusion steps, twists, and turns for molecular docking. In *Proceedings of the International Conference on Learning Representations (ICLR)*, 2023. URL <https://arxiv.org/abs/2210.01776>.
- Dalalyan, A. S. Sharp adaptive estimation of the drift function for ergodic diffusions. *Annals of Statistics*, 34(1): 291–376, 2006.
- De Bortoli, V., Thornton, J., Heng, J., and Doucet, A. Diffusion Schrödinger Bridge with Applications to Score-Based Generative Modeling. In *Advances in Neural Information Processing Systems*, 2021.

- Denis, C., Dion-Blanc, C., and Martinez, M. A ridge estimator of the drift from discrete repeated observations of the solution of a stochastic differential equation. *Bernoulli*, 27(4):2675–2713, 2021. doi: 10.3150/21-BEJ1327. URL <https://doi.org/10.3150/21-BEJ1327>.
- Dhariwal, P. and Nichol, A. Q. Diffusion models beat GANs on image synthesis. In Beygelzimer, A., Dauphin, Y., Liang, P., and Vaughan, J. W. (eds.), *Advances in Neural Information Processing Systems*, 2021. URL <https://openreview.net/forum?id=AAWuCVzaVt>.
- Florens-Zmirou, D. On estimating the diffusion coefficient from discrete observations. *Journal of Applied Probability*, 30(4):790–804, 1993.
- Franzese, G., Corallo, G., Rossi, S., Heinonen, M., Filippone, M., and Michiardi, P. Continuous-Time Functional Diffusion Processes. In *Advances in Neural Information Processing Systems*, 2023.
- Gobet, E. Lan property for ergodic diffusions with discrete observations. *Annales de l’Institut Henri Poincaré, Probabilité et Statistiques*, 38(4):651–676, 2002. doi: 10.1016/S0246-0203(02)01107-X.
- Ho, J., Jain, A., and Abbeel, P. Denoising diffusion probabilistic models. In Larochelle, H., Ranzato, M., Hadsell, R., Balcan, M., and Lin, H. (eds.), *Advances in Neural Information Processing Systems*, volume 33, pp. 6840–6851. Curran Associates, Inc., 2020. URL https://proceedings.neurips.cc/paper_files/paper/2020/file/4c5bcfec8584af0d967f1ab10179ca4b-Paper.pdf.
- Ho, J., Saharia, C., Chan, W., Fleet, D. J., Norouzi, M., and Salimans, T. Video diffusion models. In *Advances in Neural Information Processing Systems (NeurIPS)*, volume 35, pp. 8633–8646, 2022. URL <https://arxiv.org/abs/2204.03458>.
- Hyvarinen, A. and Dayan, P. Estimation of non-normalized statistical models by score matching. *Journal of Machine Learning Research*, 6(4), 2005.
- Jacod, J. Limit of random measures associated with the increments of a semimartingale. *Stochastic Processes and their Applications*, 50(1):41–60, 1994.
- Jacod, J. and Protter, P. *Discretization of Processes*, volume 67. Springer, 2012.
- Jakobsen, N. M. and Sørensen, M. Efficient estimation for diffusions sampled at high frequency over a fixed time interval. Technical Report 2015-33, CREATES, Aarhus University, 2015. URL <https://ideas.repec.org/p/aah/create/2015-33.html>.
- Jolicœur-Martineau, A., Li, K., Piché-Taillefer, R., Kachman, T., and Mitliagkas, I. Gotta go fast when generating data with score-based models, 2021.
- Karatzas, I. and Shreve, S. E. *Brownian Motion and Stochastic Calculus*, volume 113. Springer, 2 edition, 2000.
- Karras, T., Aittala, M., Aila, T., and Laine, S. Elucidating the design space of diffusion-based generative models, 2022. URL <https://arxiv.org/abs/2206.00364>.
- Kessler, M. Estimation of an ergodic diffusion from discrete observations. *Scandinavian Journal of Statistics*, 24(2):211–229, 1997.
- Kim, B. J., Kawahara, Y., and Kim, S. W. The disappearance of timestep embedding in modern time-dependent neural networks. *arXiv preprint arXiv:2405.14126*, 2024. URL <https://arxiv.org/abs/2405.14126>.
- Kingma, D. P. and Ba, J. Adam: A method for stochastic optimization. In *International Conference on Learning Representations*, 2015.
- Kolloviev, M., Ansari, A. F., Bohlke-Schneider, M., Zschiegner, J., Wang, H., and Wang, Y. Predict, refine, synthesize: Self-guiding diffusion models for probabilistic time series forecasting. In *Advances in Neural Information Processing Systems (NeurIPS) 36*, 2023.
- Kong, Z., Ping, W., Huang, J., Zhao, K., and Catanzaro, B. Diffwave: A versatile diffusion model for audio synthesis. In *International Conference on Learning Representations (ICLR) 2021*, 2021.
- Koshiyama, A., Firoozye, N., and Treleaven, P. Generative adversarial networks for financial trading strategies fine tuning and combination. *Quantitative Finance*, 21(5):797–813, 2021. doi: 10.1080/14697688.2020.1790635. URL <https://doi.org/10.1080/14697688.2020.1790635>.
- Kutoyants, Y. A. *Statistical Inference for Ergodic Diffusion Processes*. Springer, 2004. doi: 10.1007/978-1-4471-3866-2.
- Lim, H., Kim, M., Park, S., and Park, N. Regular time-series generation using SGM. In *Advances in Neural Information Processing Systems (NeurIPS) 36*, 2023.
- Lin, L., Li, Z., Li, R., Li, X., and Gao, J. Diffusion Models for Time Series Applications: A Survey, 2023.

- Lorenz, E. N. Predictability: A problem partly solved. *Proceedings of the Seminar on Predictability*, 1:1–18, 1996.
- Marie, N. and Rosier, A. Nadaraya–watson estimator for i.i.d. paths of diffusion processes. *Scandinavian Journal of Statistics*, 50(2):589–637, 2023. doi: 10.1111/sjos.12593. URL <https://onlinelibrary.wiley.com/doi/abs/10.1111/sjos.12593>.
- Mohammadi, N., Santoro, L., and Panaretos, V. M. Non-parametric Estimation for SDE with Sparsely Sampled Paths: an FDA Perspective. *Stochastic Processes and Their Applications*, 2024. doi: 10.1016/j.spa.2023.104239.
- Nadaraya, E. A. On estimating regression. *Theory of Probability & Its Applications*, 9(1):141–142, 1964.
- Oga, A. and Koike, Y. Drift estimation for a multi-dimensional diffusion process using deep neural networks. *Stochastic Processes and Their Applications*, 2023. doi: 10.1016/j.spa.2023.104240. URL <https://www.sciencedirect.com/science/article/pii/S0304414923002120>.
- Rasul, K., Seward, C., Schuster, I., and Vollgraf, R. Autoregressive denoising diffusion models for multivariate probabilistic time series forecasting. In Meila, M. and Zhang, T. (eds.), *Proceedings of the 38th International Conference on Machine Learning*, volume 139, pp. 8857–8868. PMLR, 2021.
- Rombach, R., Blattmann, A., Lorenz, D., Esser, P., and Ommer, B. High-resolution image synthesis with latent diffusion models. In *Proceedings of the IEEE/CVF Conference on Computer Vision and Pattern Recognition (CVPR)*, pp. 10684–10695, 2022. URL <https://arxiv.org/abs/2112.10752>.
- Saharia, C., Chan, W., Saxena, S., Li, L., Whang, J., Denton, E., Seyed Ghasemipour, K., Ayan, B. K., Mahdavi, S. S., Lopes, R. G., Salimans, T., Ho, J., Fleet, D. J., and Norouzi, M. Photorealistic text-to-image diffusion models with deep language understanding. In *Advances in Neural Information Processing Systems (NeurIPS)*, volume 35, pp. 36479–36494, 2022. URL <https://arxiv.org/abs/2205.11487>.
- Shen, L. and Kwok, J. Non-autoregressive conditional diffusion models for time series prediction. In *Proceedings of the 40th International Conference on Machine Learning (ICML)*, 2023.
- Shi, Y., Bortoli, V. D., Deligiannidis, G., and Doucet, A. Conditional simulation using diffusion schrödinger bridges, 2022.
- Shi, Y., De Bortoli, V., Campbell, A., and Doucet, A. Diffusion schrödinger bridge matching. In *Advances in Neural Information Processing Systems (NeurIPS)* 36, 2023.
- Shoji, I. and Ozaki, T. Estimation for nonlinear stochastic differential equations by a local linearization method. *Stochastic Analysis and Applications*, 13(1):1–25, 1995.
- Sohl-Dickstein, J., Weiss, E., Maheswaranathan, N., and Ganguli, S. Deep unsupervised learning using nonequilibrium thermodynamics. In Bach, F. and Blei, D. (eds.), *Proceedings of the 32nd International Conference on Machine Learning*, volume 37, pp. 2256–2265. PMLR, 2015. URL <https://proceedings.mlr.press/v37/sohl-dickstein15.html>.
- Song, J., Meng, C., and Ermon, S. Denoising diffusion implicit models. In *International Conference on Learning Representations*, 2021a. URL <https://openreview.net/forum?id=StlgiarCHLP>.
- Song, Y. and Ermon, S. Generative modeling by estimating gradients of the data distribution. In Wallach, H., Larochelle, H., Beygelzimer, A., d’Alche Buc, F., Fox, E., and Garnett, R. (eds.), *Advances in Neural Information Processing Systems*, volume 32. Curran Associates, Inc., 2019. URL https://proceedings.neurips.cc/paper_files/paper/2019/file/3001ef257407d5a371a96dcd947c7d93-Paper.pdf.
- Song, Y., Sohl-Dickstein, J., Kingma, D. P., Kumar, A., Ermon, S., and Poole, B. Score-based generative modeling through stochastic differential equations, 2021b. URL <https://arxiv.org/abs/2011.13456>.
- Song, Y., Sohl-Dickstein, J., Kingma, D. P., Kumar, A., Ermon, S., and Poole, B. Score-based generative modeling through stochastic differential equations. In *International Conference on Learning Representations*, 2021c. URL <https://openreview.net/forum?id=PXTIG12RRHS>.
- Starnes, A. and Webster, C. Improved performance of stochastic gradients with gaussian smoothing. In *Optimization, Learning Algorithms and Applications*, volume 2617 of *Communications in Computer and Information Science*. Springer, Cham, 2025. doi: 10.1007/978-3-032-00137-5_11.
- Taskhiro, Y., Song, J., Song, Y., and Ermon, S. CSDI: Conditional score-based diffusion models for probabilistic time series imputation. In Beygelzimer, A., Dauphin, Y., Liang, P., and Vaughan, J. W. (eds.), *Advances in Neural Information Processing Systems*, 2021. URL <https://openreview.net/forum?id=VzuIzBRDrum>.

- Tsybakov, A. B. *Introduction to Nonparametric Estimation*. Springer, 2009. doi: 10.1007/b13794.
- Vincent, P. A connection between score matching and denoising autoencoders. *Neural computation*, 23(7):1661–1674, 2011.
- Watson, D., Ho, J., Norouzi, M., and Chan, W. Learning to efficiently sample from diffusion probabilistic models, 2022. URL <https://openreview.net/forum?id=LOz0xDpw4Y>.
- Watson, G. S. Smooth regression analysis. *Sankhyā: The Indian Journal of Statistics, Series A*, 26(4):359–372, 1964.
- Xu, M., Powers, A. S., Dror, R. O., Ermon, S., and Leskovec, J. Geometric latent diffusion models for 3d molecule generation. In *Proceedings of the 40th International Conference on Machine Learning (PMLR)*, volume 202, pp. 38592–38610. PMLR, 2023. URL <https://proceedings.mlr.press/v202/xu23n.html>.
- Xu, Y., Ma, X., Zhang, J., Chen, Y., Wang, Y., Zhao, H., Wang, Y., Zhang, C., Ji, R., and Xu, H. Fast sampling of diffusion models with exponential integrator. *arXiv preprint arXiv:2204.13902*, 2022. URL <https://arxiv.org/abs/2204.13902>.
- Yan, T., Zhang, H., Zhou, T., Zhan, Y., and Xia, Y. Scoregrad: Multivariate probabilistic time series forecasting with continuous energy-based generative models, 2021. URL <https://arxiv.org/abs/2106.10121>.
- Zhang, L., Ma, H., Zhu, X., and Feng, J. Preconditioned Score-based Generative Models. In *Advances in Neural Information Processing Systems*, 2023.
- Zhao, Y., Liu, Y., and Hoffmann, M. Drift estimation for diffusion processes using neural networks based on discretely observed independent paths. *arXiv preprint arXiv:2511.11161*, 2025. URL <https://arxiv.org/abs/2511.11161>.

A. Sensitivity to forward noising process

In this section, we motivate why the forward noising process $q_\tau(X_\tau|X_0)$ needs to be carefully chosen to ensure our denoising estimator (19) accurately recovers the drift function.

Recall the transition kernel for the VPSDE noising process,

$$q_\tau(x_\tau | X_0) = \mathcal{N}(x_\tau; \beta_\tau X_0, \sigma_\tau^2 I),$$

where $\beta_\tau = \exp(-0.25\tau^2(\gamma_1 - \gamma_0) - 0.5\tau\gamma_0)$ and $\sigma_\tau^2 = 1 - \beta_\tau^2$. (Song et al., 2021b) define an alternative noising process (the Variance Exploding SDE), which takes samples $X_0 \sim p_0$ and diffuses them with the forward transition density,

$$q_\tau^{\text{VE}}(x_\tau | X_0) = \mathcal{N}(x_\tau; X_0, \phi_\tau^2 I), \quad (24)$$

where $\phi_\tau = \phi_0(\phi_1/\phi_0)^\tau, \forall \tau \in [\epsilon, 1]$. As in the VPSDE process, $\epsilon > 0$ is chosen to avoid vanishing variance as $\tau \rightarrow 0$. However, in contrast to the VPSDE process, where noise variance σ_τ^2 increases smoothly and saturates at 1, the noise variance ϕ_τ^2 in VESDE increases exponentially. Under uniform sampling in τ , this concentrates most training mass at low marginal noise levels. Consequently, the denoising estimator is trained predominantly in high signal-to-noise regimes, where learning the denoising target is hardest. By comparison, the VPSDE distributes training more evenly across signal-to-noise ratios. As such, given the same maximum noise levels $\phi_1 = \sigma_1$, the VESDE process spends more time in lower-noise regimes, where denoising is hardest.

We extend the experiments in Section 4.3 by diffusing the observed increments X_0 with the VESDE noising kernel in (24). We consider two VESDE variants. In VESDE-Matched, we set $\phi_1 = 1$ to match the maximum marginal variance in the VPSDE. In VESDE-Larger, we increase the maximum marginal noise to $\phi_1 = 15$ to compensate for the concentration of training mass at low noise levels under VESDE-Matched. In both cases, $\phi_0 = 0.03$, and we set $\epsilon = 6.5 \times 10^{-2}$ in VESDE-Matched and $\epsilon = 5 \times 10^{-2}$ in VESDE-Larger in both training and evaluation to ensure the minimum marginal variance for both processes is identical to that of the VPSDE process in Section 4.3.

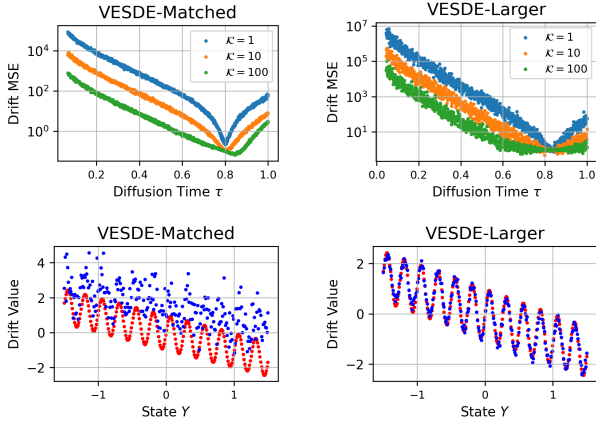


Figure 7. The top panels shows the drift error $e^2(\tau)$ when estimating $\mu^{(1)}$; the bottom panels compares the **true** drift to the **estimated** drift at $\tau = 1$. Positions Y are uniformly spaced between $[-1.5, 1.5]$, covering 99% of the training distribution.

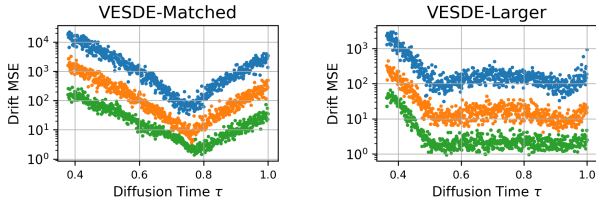


Figure 8. Drift error $e^2(\tau)$ for $\mu^{(2)}$ with $D = 8$ for VESDE-Matched (left) and VESDE-Larger (right).

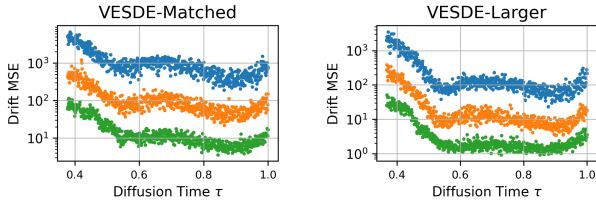


Figure 9. Drift error $e^2(\tau)$ for $\mu^{(2)}$ with $D = 12$ for VESDE-Matched (left) and VESDE-Larger (right).

As in the VPSDE case, Figures 7-9 show increasing \mathcal{K} reduces the drift MSE uniformly across τ for both VESDE variants. However, for fixed \mathcal{K} , VESDE-Matched exhibits uniformly larger errors than VESDE-Larger. This gap is most pronounced for large diffusion times, where the forward process in VESDE-Larger has higher variance. Taken together, these results show that matching maximum marginal variance is insufficient for accurate drift estimation, and that effective denoising requires adequate coverage of high noise regimes during training.

B. Denoising Network Architecture

The architecture described in this section corresponds to the denoising network used for DN. The variant DN-Lin is obtained by removing the *MLPStateMapper* component (see Figure 11 and replacing it with a fully connected mapping of matching output dimension, and no other module is

changed.

The network for DN is constructed such that the output is given by,

$$D_\theta(\tau, X_\tau, Y) = f_\theta(Y) + g_\theta(X_\tau, Y) + m_\theta(g_\theta, \tau).$$

Figure 10 summarises the main components of the denoiser network architecture. The path followed by modules highlighted in blue represents the implementation of g_θ as a sequence of 1D convolutional neural networks and a single 1D convolutional residual layer. The function m_θ , highlighted in orange, conditions the network on the diffusion time through a fully connected residual layer. The architecture for m_θ is motivated by the vanishing dependence of traditional diffusion models on the diffusion time (Kim et al., 2024).

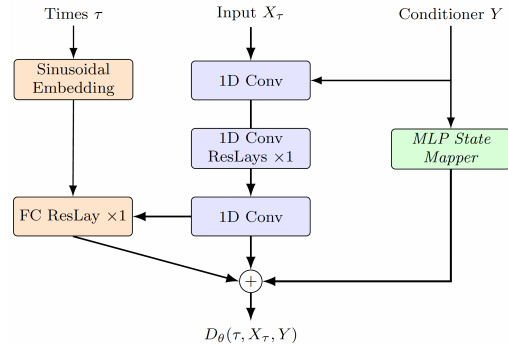


Figure 10. Score network D_θ used for DN.

In prior diffusion model architectures, the conditioning mapping f_θ is often implemented using sequence-based architectures such as Long Short-Term Memory (LSTM) networks or Transformers (Yan et al., 2021; Corso et al., 2023; Lim et al., 2023; Saharia et al., 2022). These architectures maintain an internal state that evolves with the history of observed inputs. In this paper, f_θ is implemented using the *MLPStateMapper*, see Figure 11, which defines a non-linear feature mapping of the observed state Y without maintaining a recurrent or attention-based state. This design reflects the Markovian dependence structure induced by the data-generating SDE in (1). The mapping is constructed by combining multiple feature pathways: element-wise polynomial features (Y, Y^2, Y^3), a learned global non-linear transformation implemented as a linear-ELU block, and Fourier features. The Fourier features are modulated by a learnable scalar gate, allowing their contribution to be adaptively scaled during training. All feature components are concatenated and passed through a two-layer fully connected network to produce the final output in \mathbb{R}^D .

The number of trainable parameters in D_θ scales as $T(D) = 2D^2 + \mathcal{O}(D) + \mathcal{O}(1)$. The quadratic dependence on the time-series dimensionality arises from the first 1D convolution in g_θ , see Figure 10, although the constant term in $T(D)$ is much larger than the linear or quadratic terms.

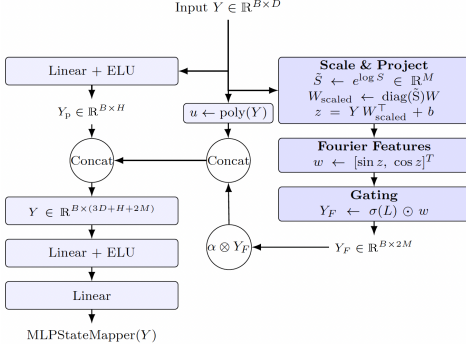


Figure 11. *MLPStateMapper* module. It provides an inductive bias towards polynomial and Fourier features, which can be learned from the data.

C. Baselines

C.1. IID Nadaraya-Watson Estimator

In (Marie & Rosier, 2023), the authors improve the standard Nadaraya-Watson estimator for the drift function by averaging over \mathcal{I} IID sample paths observed discretely \mathcal{J} times. Assuming each path is defined on the same uniform time grid with $\Delta = t_{j+1} - t_j$, the discrete-time estimator for the drift function is given by,

$$\widehat{b}_{\mathcal{J}, \mathcal{I}, h}(y) = \frac{\widehat{b}_{\mathcal{J}, \mathcal{I}, h}(y)}{\widehat{f}_{\mathcal{J}, \mathcal{I}, h}(y)}, \quad (25)$$

where,

$$\widehat{f}_{\mathcal{J}, \mathcal{I}, h}(y) = \frac{1}{\mathcal{J}\mathcal{I}} \sum_{i=1}^{\mathcal{I}} \sum_{j=0}^{\mathcal{J}-1} K_h(Y_{t_j}^{(i)} - y), \quad (26)$$

and,

$$\widehat{b}_{\mathcal{J}, \mathcal{I}, h}(y) = \frac{1}{\mathcal{I}} \sum_{i,j} K_h(Y_{t_j}^{(i)} - y) Z_{t_j}^{(i)}, \quad (27)$$

and $Y_{t_j}^{(i)}$, $Z_{t_j}^{(i)}$ are defined in Section 4.1. In our experiments, we choose $K_h(y) = (2\pi h^{2D})^{-0.5} \exp[-0.5h^{-2} \|y\|_2^2]$.

To choose the optimal bandwidth h , one finds the bandwidth which minimises the leave-one-out-cross validation criterion,

$$CV(h) = \sum_{i=1}^{\mathcal{I}} \sum_{j=0}^{\mathcal{J}-1} \left[\widehat{b}_{\mathcal{J}, \mathcal{I}, h}^{-(-i)}(Y_{t_j}^{(i)})^2 \Delta - 2\widehat{b}_{\mathcal{J}, \mathcal{I}, h}^{-(-i)}(Y_{t_j}^{(i)})(Y_{t_{j+1}}^{(i)} - Y_{t_j}^{(i)}) \right]$$

where $\widehat{b}_{\mathcal{J}, \mathcal{I}, h}^{-(-i)}$ is the leave-one-out drift estimator.

Under the regularity assumptions of (Marie & Rosier, 2023), parameterised by a spatial smoothness index $\beta \geq 1$

of the marginal density $q_t(\cdot)$ of (1), and a discretization parameter $\epsilon \in [0, 1)$, risk control in expected squared L_2 error is achieved via the truncated estimator,

$$\widetilde{b}_{\mathcal{J}, \mathcal{I}, h} = \widehat{b}_{\mathcal{J}, \mathcal{I}, h} \mathbb{1}(\widehat{f}_{\mathcal{J}, \mathcal{I}, h} > m/2),$$

where $m > 0$ is a lower bound on the time-averaged marginal density, f . Under these conditions, the estimator over a compact domain $[A, B]$ satisfies the risk bound,

$$\mathbb{E} \|\widetilde{b}_{\mathcal{J}, \mathcal{I}, h} - b\|_{f, A, B} = \mathcal{O}\left((T - t_0)\mathcal{I}^{-1} + h^{2\beta} + \mathcal{I}^{-1}h^{-1} + \mathcal{I}\mathcal{J}h^{3+\epsilon}\right).$$

As noted in (Marie & Rosier, 2023), when $T > 1$, choosing $t_0 \in [1, T - 1]$ removes the time-dependent factors in the risk rate. In the worst-case regime, $h < 1$, the rate is maximised at $\beta = 1$, and if the true drift function is bounded, one may take $\epsilon = 0$.

C.2. IID Ridge Estimator

The IID Ridge estimator in (Denis et al., 2021) is a non-parametric estimator of a one dimensional drift function using B -splines. Letting $L_{\mathcal{I}}, K_{\mathcal{I}}, M > 0$, and end points $A_{\mathcal{I}} = -B_{\mathcal{I}} < 0$, (Denis et al., 2021) define a sequence of knots,

$$u_s = \begin{cases} A_{\mathcal{I}}, & s = -M, \dots, 0, \\ A_{\mathcal{I}} + \frac{s}{K_{\mathcal{I}}}(B_{\mathcal{I}} - A_{\mathcal{I}}), & s = 1, \dots, K_{\mathcal{I}}, \\ B_{\mathcal{I}}, & s = K_{\mathcal{I}} + 1, \dots, K_{\mathcal{I}} + M. \end{cases}$$

Denoting the spline basis by $B_{s, M, u}$, and the projection subspace as $S_{K_{\mathcal{I}}, M, u} = \text{span}\{(B_{s, M, u}) \forall s \in \{-M, \dots, K_{\mathcal{I}} - 1\}\}$, such that $\dim(S_{K_{\mathcal{I}}, M, u}) = K_{\mathcal{I}} + M$, then for any $y \in [A_{\mathcal{I}}, B_{\mathcal{I}}]$, the drift estimator is given by,

$$\widehat{b}_{\mathcal{I}, \mathcal{J}}(y) = \sum_{s=-M}^{K_{\mathcal{I}}-1} \widehat{a}_s B_{s, M, u}(y) \quad (28)$$

Defining the entries in the matrix B as $B_{r, s} = B_{s, M, u}(Y_{t_j}^{(i)})$ with row index $r = \mathcal{J}(i - 1) + j$, and $Z \in \mathbb{R}^{\mathcal{I}\mathcal{J}}$ where $Z_r = \Delta^{-1}(Y_{t_{j+1}}^{(i)} - Y_{t_j}^{(i)})$, the solution to (28) satisfies $\widehat{a} = (B^T B)^{-1} B^T Z$ if $B^T B$ is full column rank and $\|\widehat{a}\|_2^2 \leq (K_{\mathcal{I}} + M)L_{\mathcal{I}}$. Alternatively, letting $\widehat{\lambda}$ be the unique solution to $\|(B^T B + \lambda I)^{-1} B^T Z\|_2^2 = (K_{\mathcal{I}} + M)L_{\mathcal{I}}$, the solution is given by $\widehat{a} = (B^T B + \lambda I)^{-1} B^T Z$.

Assuming only the necessary conditions for the existence and uniqueness of a strong solution to (1), (Denis et al., 2021) show that the risk bound is controlled by a bias term and a variance term which scales as $(\dim(S_{K_{\mathcal{I}}, M, u})\mathcal{I}^{-1})^{-0.5} + \Delta$. Under further regularity conditions for the drift function, (Denis et al., 2021) obtain

a risk bound of order $(\ln^2 \mathcal{I}/\mathcal{I})^{\frac{2\beta}{2\beta+1}}$.

C.3. IID Hermite Projection Estimator

Comte and Genon-Catalot (Comte & Genon-Catalot, 2020) derive a nonparametric estimator for a one dimensional drift function using a least-squares projection onto a subspace spanned by Hermite polynomials. Given the first m Hermite polynomial basis functions $(h_k)_{k=0}^{m-1}$, and \mathcal{I} sample paths observed continuously on $t \in [0, T]$, the drift estimator is given by

$$\hat{b}_m(y) = \sum_{k=0}^{m-1} \hat{\theta}_k h_k(y),$$

where $(\hat{\theta}_k)_{k=0}^{m-1}$ is the vector of parameters obtained via the least-squares projection onto the space spanned by the Hermite polynomials, h_k ,

$$\hat{\theta}_k = e_k^T \hat{\Phi}_m^{-1} \hat{Z}_m. \quad (29)$$

where e_k is the k -th canonical basis vector. In (29), $\hat{\Phi}_m \in \mathbb{R}^{m \times m}$, $\hat{Z}_m \in \mathbb{R}^m$ are defined as,

$$\hat{\Phi}_{m,(u,v)} = \frac{1}{\mathcal{I}T} \sum_{i=1}^{\mathcal{I}} \int_0^T h_v(Y_s^{(i)}) h_u(Y_s^{(i)}) ds$$

$$\hat{Z}_{m,u} = \frac{1}{\mathcal{I}T} \sum_{i=1}^{\mathcal{I}} \int_0^T h_u(Y_s^{(i)}) dY_s^{(i)},$$

where $u, v \in \{0, \dots, m-1\}$.

To find the optimal truncation level m , (Comte & Genon-Catalot, 2020) propose to optimise

$$\hat{m} = \arg_{m \in \mathcal{M}} \min \left[-\left\| \hat{b}_m \right\|_{\mathcal{I}}^2 + \kappa \left\| \hat{\Phi}_m^{-1} \hat{\Phi}_{m,\sigma^2} \right\|_{op} \frac{m}{\mathcal{I}T} \right],$$

where $\mathcal{M} = \left\{ m : m \leq 10, m \left\| \hat{\Phi}_m^{-1} \right\|_{op}^{1/4} \leq \mathcal{I}T \right\}$, see (Comte & Genon-Catalot, 2020) for notation.

In the case of continuous observations of the sample paths and bounded diffusion coefficient, Theorem 1 in (Comte & Genon-Catalot, 2020) proves the risk bound on $\hat{b}_{\hat{m}}$ is order $\mathcal{O}(1/\mathcal{I}T)$.

C.4. Neural-Network Based Benchmark Estimators

The benchmark FC is constructed as a fully-connected feedforward network with ReLU activation functions, as in (Zhao et al., 2025). The number of layers and the width of each layer are chosen based on the empirical results in the code repository by (Zhao et al., 2025).

However, for a fixed dataset, the number of parameters in FC can be several orders of magnitude smaller than our denoising network D_θ . The benchmark FC⁺ increases the

depth of FC until the number of parameters exceeds the parameter count in D_θ . Architectural details achieving this constraint are fixed deterministically and reported in the code repository.

We implement FC⁺-Conv as the sum of a fully-connected backbone and a convolutional module,

$$(\text{FC}^+\text{-Conv})_\theta(Y) \equiv \text{FC}_\theta(Y) + g_\theta(Y),$$

The convolutional module g_θ follows the same design pattern as the convolutional path in DN, but with the first channel dimension adjusted to account for the absence of noisy inputs X_τ . The fully-connected backbone of FC⁺-Conv is resized relative to FC⁺ so that the *total* number of trainable parameters of FC⁺-Conv matches that of D_θ for the same dataset.

D. Estimator hyperparameter selection

D.1. IID Hermite Estimator

Figure 12 shows how the number of basis functions for the Hermite estimator in (Comte & Genon-Catalot, 2020) is selected by optimising $E_1^{(\mu)}$. As suggested in (Comte & Genon-Catalot, 2020), increasing the number of basis functions beyond $m = 10$ yields small marginal improvements in estimator accuracy; nevertheless, we conduct a grid search for $m > 10$ for completeness.

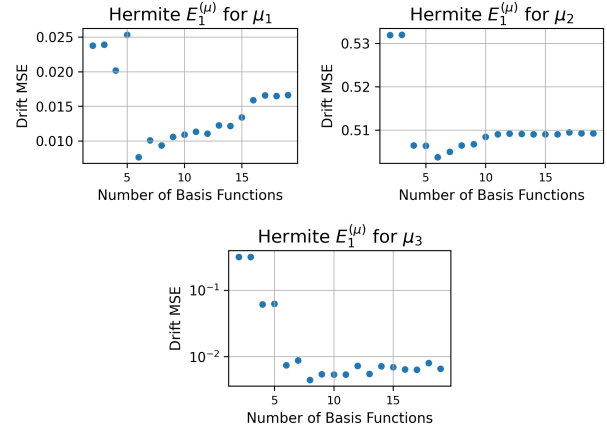


Figure 12. Hermite drift error $E_1^{(\mu)}$, against number of basis functions. From left to right, top to bottom, the estimation for μ_1 , μ_2 , μ_3 .

D.2. IID Ridge Estimator

Figure 13 shows how the number of subspace dimensions for the Ridge estimator from (Denis et al., 2021) is chosen by minimising $E_1^{(\mu)}$. The Ridge estimator requires a higher B -spline dimension to accurately estimate μ_2 , plausibly due to the presence of a high-frequency sinusoidal component in the drift function. In contrast, for μ_1, μ_3 , a relatively small number of B -splines are sufficient for ac-

curate drift recovery.

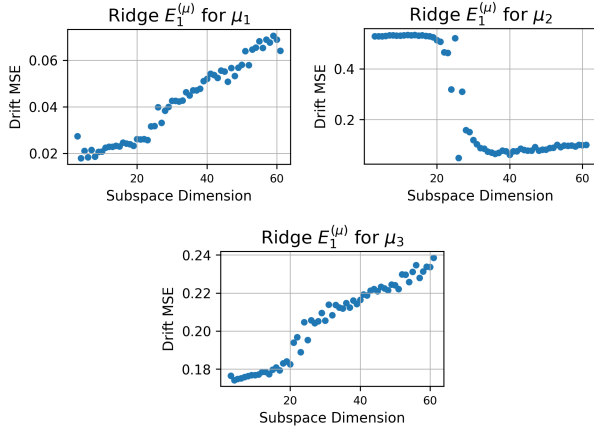


Figure 13. Ridge drift error $E_1^{(\mu)}$, against number of basis functions. From left to right, top to bottom, the estimation for μ_1 , μ_2 , μ_3 .

D.3. IID Nadaraya Estimator

Figures 14 and 15 illustrate how the bandwidth is chosen for the Nadaraya-Watson estimator when estimating μ_4 and μ_5 . For small bandwidths, the Nadaraya estimator discards many training samples, leading to large errors. As the bandwidth increases, the error decreases until it rises again once the estimator enters an over-diffuse regime in which all training points are weighted uniformly. Figure 15 shows that the optimal bandwidth increases slightly with dimension, as expected.

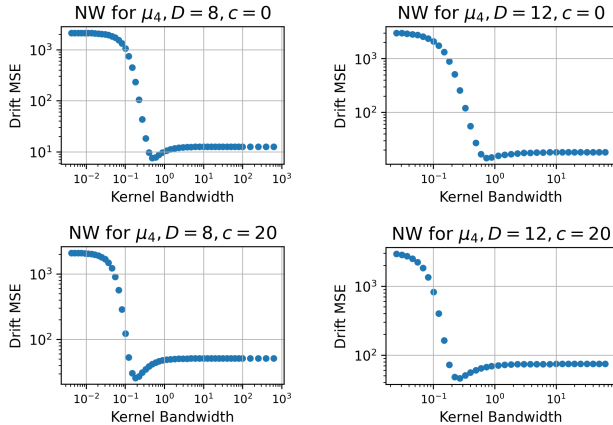


Figure 14. Nadaraya drift error $E_1^{(\mu)}$ versus bandwidth h for estimation of μ_4 .

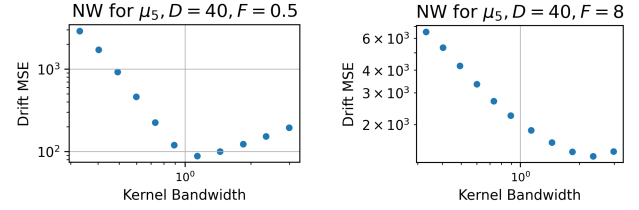
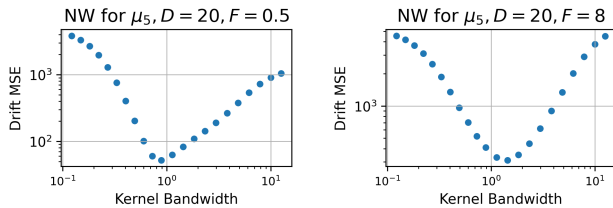


Figure 15. Nadaraya drift error $E_1^{(\mu)}$ versus bandwidth h for estimation of μ_5 . Top panels show $D = 20$, $F \in \{0.5, 8\}$ (left to right); bottom panels show $D = 40$, $F \in \{0.5, 8\}$.

D.4. Denoising Estimator

We train the network D_θ with the *MLPStateMapper* module from Figure 11 using Adam (Kingma & Ba, 2015) with an initial learning rate of 10^{-2} . We allow the learning rate to decrease by a constant factor of 0.9 whenever the training loss fails to improve for 60 consecutive epochs, setting the minimum learning rate at 10^{-3} . The output weights in g_θ , m_θ are initialised to zero. For the conditional diffusion model hyperparameters, we set $\epsilon = 10^{-3}$, $S = 10^4$, $\gamma_0 = 0$, $\gamma_1 = 20$. We train on a single NVIDIA GeForce RTX 3090 GPU (24 GiB of memory), using Pytorch 2.7 and CUDA 12.4 with driver 550.54.15.

All denoising networks are trained until the validation error $E_{256}^{(\mu)}$ has stopped improving for 100 epochs, as illustrated in Figure 16 for a selection of drift classes. In red, we show the value of $E_1^{(\mu)}$ evaluated at each epoch, suggesting the denoising objective closely matches the learning error in the drift.

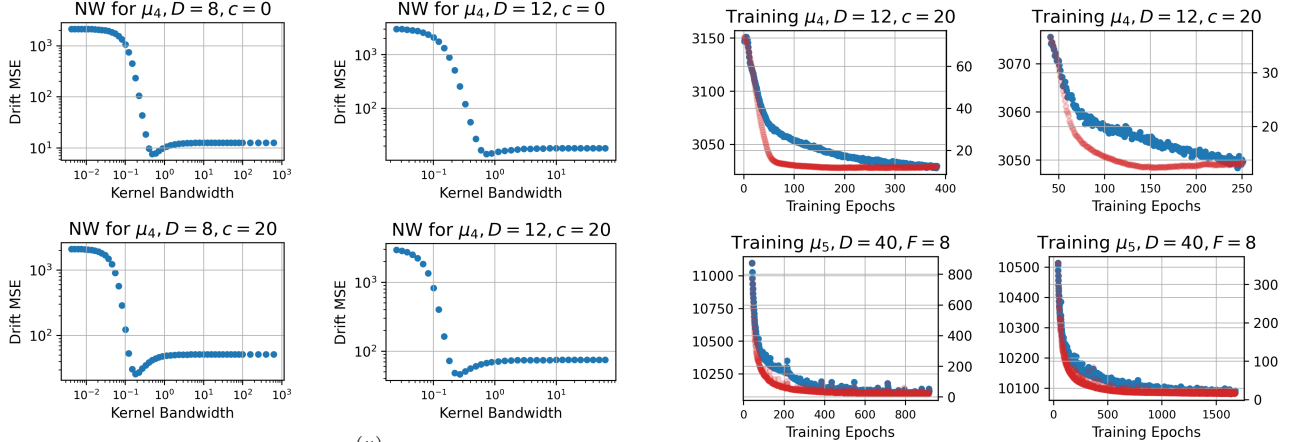


Figure 16. Training loss and $E_1^{(\mu)}$ loss for DN (left panels), and DN-Lin (right panels). Left scale shows training loss, right scale shows validation loss.

Figure 17 shows the batch-averaged norm of the gradients of the network output $D_\theta(\tau, X_\tau, Y)$ during training of DN and DN-Lin. Across the selected drift classes, we observe that the gradients with respect to each of the inputs do not vanish across epochs. Figure 18 shows the batch-averaged ratio $\|m_\theta\| / \|D_\theta\|$ generally increases during training, suggesting the contribution of the diffusion

time embedding grows before the model selection occurs. Taken together, Figures 17 and 18 confirm that the architecture in Appendix B does not collapse to standard regression using Y .

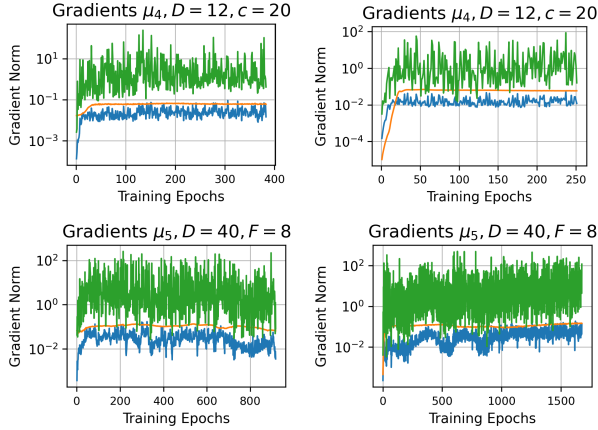


Figure 17. Training-time gradient norms with respect to **diffusion time**, X_τ , and Y . Left panels show DN, right panels show DN-Lin.

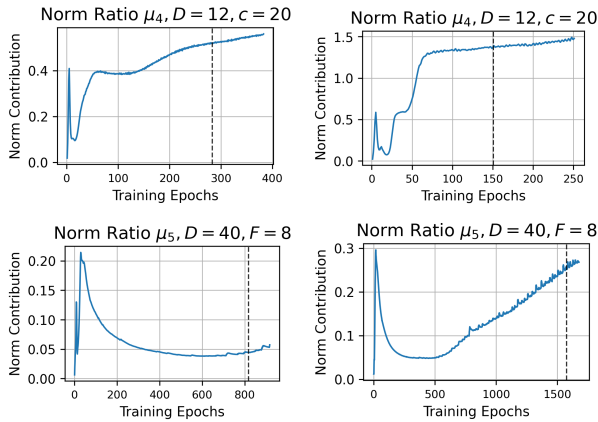


Figure 18. Relative norm of m_θ to network output D_θ during training. Left panels show DN, right panels show DN-Lin. Vertical line indicates model selection epoch.

E. Kernel Drift Estimators in High Dimensions

For completeness, Table 6 shows the out-of-sample performance of the Nadaraya-Watson estimator from (Marie & Rosier, 2023). As highlighted in Section 5.2 and Appendix C, the kernel bandwidth is chosen through a grid search to minimise $E_1^{(\mu)}$.

Table 6 shows that the Nadaraya-Watson estimator performs poorly in high dimensions when compared to all baselines reported in Section 5.4.2.

Table 6. Final-time out-of-sample drift error $E_1^{(\mu)}$ for kernel (NW) estimators.

(a) μ_4			(b) μ_5		
c	D	NW	F	D	NW
0	8	14.454	$\frac{1}{2}$	20	186.914
	12	26.544		40	220.199
20	8	292.256	8	20	8493
	12	231.207		40	17237

F. Sensitivity to number of training trajectories

We quantify the sensitivity of the final-time in-sample error $E_1^{(\mu)}$ to a tenfold reduction in the number of training paths, from $I = 10^3$ to $I = 10^2$. Training procedure is identical to that outlined in Section 5.2, and we report the in-sample drift error $E_1^{(\mu)}$ for each test drift from Section 5.3. We define the relative change in the error as $|E_1^{(\mu)}(10^2) - E_1^{(\mu)}(10^3)| / E_1^{(\mu)}(10^3)$.

Tables 7-9 summarize the results for the estimators (DN), (DN-Lin), and FC^+ -Conv, for the bistable potential (μ_4) and Lorenz 96 (μ_5) drift families. We exclude the FC and FC^+ baselines from this section, as they are not competitive in the corresponding in-sample regimes in Section 5.4.

Table 7. In-sample drift error $E_1^{(\mu)}$ of DN with 10^2 training paths, for μ_4 and μ_5 . Relative change is computed with respect to the corresponding 10^3 -path results reported in Section 5.4.

Drift	Param	D	$E_1^{(\mu)}(10^2)$	Rel. change
μ_4	$c = 0$	8	5.483	4.24
		12	10.415	5.20
	$c = 20$	8	17.188	1.03
		12	19.638	0.84
μ_5	$F = 0.5$	20	22.629	3.65
		40	38.291	2.99
	$F = 8$	20	60.648	5.36
		40	115.197	5.44

Table 8. In-sample drift error $E_1^{(\mu)}$ of DN-Lin with 10^2 training paths, for μ_4 and μ_5 .

Drift	Param	D	$E_1^{(\mu)}(10^2)$	Rel. change
μ_4	$c = 0$	8	12.517	0.80
		12	19.913	0.76
	$c = 20$	8	11.935	0.16
		12	15.483	0.13
μ_5	$F = 0.5$	20	19.172	5.13
		40	28.209	2.63
	$F = 8$	20	53.942	8.42
		40	85.047	5.97

 Table 9. In-sample drift error $E_1^{(\mu)}$ of FC⁺-Conv with 10^2 training paths, for μ_4 and μ_5 .

Drift	Param	D	$E_1^{(\mu)}(10^2)$	Rel. change
μ_4	$c = 0$	8	11.425	1.93
		12	19.065	2.02
	$c = 20$	8	21.307	1.36
		12	45.019	2.20
μ_5	$F = 0.5$	20	18.383	3.93
		40	30.650	1.57
	$F = 8$	20	47.310	3.12
		40	94.261	4.78

Across all settings, reducing the number of training paths from $I = 10^3$ to $I = 10^2$ leads to a consistent increase in final-time in-sample error. While the relative ordering of the estimators is not preserved relative to Section 5.4, the observed changes reflect differences in the magnitude of degradation, rather than the collapse of any particular estimator, as no estimator exhibits abrupt divergence behaviour under reduced data.

G. Extended Out-of-Sample Results

We report additional results for the bistable drift μ_4 , and we extend the main comparison in Section 5.4.2 to a higher dimension ($D = 20$) for the case $c = 20$. Tables 10 and 11 include the denoising estimator (DN) and the convolutional baseline (FC⁺-Conv). We additionally introduce (FC⁺-Conv-MLPSM), in which the fully connected layers in FC⁺-Conv are replaced by the *MLPStateMapper* in DN. Training and evaluation procedures are identical to those reported in Section 5.2.

 Table 10. Final-time OOS drift error $E_{20}^{(\mu)}$, for $\mu_4, c = 0$.

c	D	DN	FC ⁺ -Conv-MLPSM	FC ⁺ -Conv
0	8	<u>1.546</u>	0.793*	9.744
	12	<u>2.314</u>	1.695*	8.344

 Table 11. Final-time OOS drift error $E_{20}^{(\mu)}$, for $\mu_4, c = 20$.

c	D	DN	FC ⁺ -Conv-MLPSM	FC ⁺ -Conv
20	8	50.919*	124.972	<u>76.061</u>
	12	81.721*	<u>111.634</u>	121.379
	20	182.566*	278.475	<u>245.536</u>

In the separable regime ($c = 0$), the *MLPStateMapper* leads to improved performance of standard regression baselines, as (FC⁺-Conv-MLPSM) lower OOS errors than its denoising-based counterpart. In contrast, in the non-separable regime ($c = 20$), FC⁺-Conv-MLPSM consistently underperforms DN across all dimensions, indicating that architectural bias alone is insufficient to recover the observed OOS gains.

H. Sensitivity to time series sampling frequency

As motivated in the Introduction, in increment-based regression, decreasing the sampling frequency Δ can lead to high variance estimators. In this section, we study the stability of the denoising estimator to different sampling frequencies Δ and compare it to the estimator FC⁺-Conv-MLPSM (see Appendix G). We consider the bi-stable drift μ_4 in both separable ($c = 0$) and non-separable ($c = 20$) regimes. We exclude the Lorenz 96 system from this analysis, as its behaviour is dominated by advective dynamics, making a direct comparison of sampling-frequency effects less informative.

 Table 12. Final time out-of-sample error $E_{20}^{(\mu)}$ for μ_4 and DN and FC⁺-Conv-MLPSM for different sampling frequencies Δ .

c	Δ	DN	FC ⁺ -Conv-MLPSM
0	64^{-1}	0.953	0.784
	256^{-1}	1.546	0.793
	1024^{-1}	1.582	0.764
20	64^{-1}	119.032	92.415
	256^{-1}	50.919	124.972
	1024^{-1}	90.617	162.930

Table 12 shows that out-of-sample performance depends on the sampling frequency Δ for both estimators, exhibiting non-monotone behaviour as Δ decreases. In the non-separable regime, FC⁺-Conv-MLPSM performs better at coarser sampling ($\Delta = 1/64$) than at finer sampling ($\Delta = 1/1024$), while the denoising estimator DN remains superior as Δ is reduced.

I. Feasible Model Validation

We consider a feasible model validation strategy for denoising-based estimators DN, DN-Lin. The neural network-based baselines in Section 5.4 are trained on (14)

and the best model is selected by early stopping based on the drift error $E_1^{(\mu)}$. Since this requires knowledge of the true drift, we propose an alternative that does not require oracle access to the drift.

In particular, we define the validation error using the training objective (14), evaluated on $\mathcal{I} = 50$ held out paths. We report the out-of-sample performance of DN, DN-Lin using oracle and feasible validation strategies in Tables 13-14 below.

Table 13. Final-time out-of-sample drift error $E_{20}^{(\mu)}$, for DN under oracle and feasible validation.

Drift	Param	D	Oracle	Feasible
μ_4	$c = 0$	8	1.546	3.361
		12	2.314	3.290
	$c = 20$	8	50.919	50.218
		12	81.721	78.356
μ_5	$F = 0.5$	20	8.718	12.105
		40	12.198	10.680
	$F = 8$	20	3973.37	1854.08
		40	1243.11	1356.77

Table 14. Final-time out-of-sample drift error $E_{20}^{(\mu)}$, for DN-Lin under oracle and feasible validation.

Drift	Param	D	Oracle	Feasible
μ_4	$c = 0$	8	11.800	18.327
		12	16.616	25.849
	$c = 20$	8	67.297	64.894
		12	115.750	109.155
μ_5	$F = 0.5$	20	12.024	10.008
		40	11.134	14.835
	$F = 8$	20	172.783	346.931
		40	332.905	371.282

Across the settings considered, Tables 13 and 14 show feasible validation selects models of the same order of performance as oracle selection for the same estimator, without inducing catastrophic outcomes. Occasional cases where feasible validation yields an estimator with lower out-of-sample error than oracle selection are expected, since the oracle criterion targets drift recovery under the in-sample distribution, which can be significantly different from the out-of-sample distribution. These results indicate that feasible validation can be sufficient for model selection in practice, without relying on access to the true drift.